PERGAMON

Atmospheric Environment 36 (2002) 5067–5079

ATMOSPHERIC ENVIRONMENT

www.elsevier.com/locate/atmosenv

Comparisons of model simulations with observations of mean flow and turbulence within simple obstacle arrays

S.R. Hanna[a,*], S. Tehranian[a], B. Carissimo[a,b], R.W. Macdonald[c], R. Lohner[a]

[a] *School of Computational Sciences, George Mason University, MS 5C3, 4400 University Drive, Fairfax, VA 22030-4444, USA*
[b] *Electricite de France, Chatou, France*
[c] *Department of Mechanical Engineering, University of Waterloo, Waterloo, Ont., Canada N2H-3T2*

Received 2 January 2002; accepted 1 July 2002

Abstract

A three-dimensional numerical code with unstructured tetrahedral grids, the finite element flow solver (FEFLO), was used to simulate the mean flow and the turbulence within obstacle array configurations consisting of simple cubical elements. Model simulations were compared with observations from a hydraulic water flume at the University of Waterloo. FEFLO was run in large eddy simulation mode, using the Smagorinsky closure model, to resolve the larger scales of the flow field. There were four experiment test cases consisting of square and staggered arrays of cubical obstacles with separations of 1.5 and 0.5 obstacle heights. The mean velocity profile for the incoming neutral boundary layer was approximated by a power law, and the turbulent fluctuations in the approach flow were generated using a Monte Carlo model. The numerical simulations were able to capture, within 40% on average, the general characteristics of the mean flow and the turbulence, such as the strong mean wind shears and the maximum turbulence at the elevation of the obstacles and the nearly constant mean wind and the 50% reduction in the turbulent velocity within the obstacle canopy. As expected, the mean wind speeds were significantly decreased (by about a factor of two or three) in the array with closer obstacle packing. It was found that, a "street canyon" effect was more obvious for the square arrays, with higher flow speeds in between the obstacles, than for the staggered arrays.

Keywords: Urban canopy; Wind flow in urban area; Turbulence in urban area; Building effects

1. Introduction

The transport and dispersion of toxic gases resulting from accidental or intentional releases within an urban area are of great concern to public health and defense officials, since such releases pose the gravest threat to the greatest number of people. For near-ground releases in the near-field region, where most of the pollution would be located between buildings, the wind flow and dispersion are site-dependent and are highly influenced by the details of the positions of the buildings and the vortex systems that exist near them. In order to better understand the transport and dispersion of pollutants in or near an urban area, it is useful to understand the complex flow patterns due to the interactions of the wind with a building or with clusters of buildings. Over the past few years, several numerical modeling studies of this problem have been carried out by, for example, Dawson et al. (1991), Letellier et al. (2000), Calhoun et al. (2000), Kastner-Klein and Plate (1999), and DeCroix et al. (2000). The objective of the current study is to use a state-of-the-art unstructured tetrahedral grid model, the finite element flow solver (FEFLO, see Lohner et al., 2001), to attempt to better simulate the flow and dispersion around building obstacles. The accuracies of the numerical simulations are investigated

*Corresponding author. Tel.: +1-703-993-1992; fax: +1-703-993-1980.
E-mail address: shanna@gmu.edu (S.R. Hanna).

1352-2310/02/$ - see front matter
PII: S1352-2310(02)00566-6

using hydraulic water flume observations reported by Macdonald et al. (2000).

The primary characteristics of the flow patterns around an isolated building or obstacle include the displacement zone at the upwind face of the obstacle, the cavity or wake or recirculation zone in the lee of the obstacle, and the wake zone downwind of the cavity (Hosker, 1984; Snyder and Lawson, 1994). As discussed by Oke (1987) and Baik and Kim (1999), the flow patterns over groups of obstacles may be distinguished by the amount of interaction between the vortex system or cavity or wake that has developed behind the upwind building obstacle and the small vortex generated in front of the downwind obstacle. The height and width of the obstacles and the spacing between obstacles are crucial factors in determining the flow pattern.

For obstacles separated by five or more obstacle heights, H, the cavity or wake generated by the upwind obstacle and the next downwind obstacle are minimal. For separations of two to five H, the obstacles are closer together so that the downwind obstacle disturbs the wake that is in the lee of the upwind obstacle. Finally if the obstacles are close enough and are of the same height, the bulk of the flow will not enter the "canyon" between the obstacles and a stable vortex will be established between the obstacles.

Turbulent eddies and streamlines around sharp-edged obstacles such as buildings can introduce local variations in pollutant concentrations that may be quite different from that estimated by simple models such as the standard Gaussian diffusion model. Empirical correlations suggested by Hosker (1984) and others are only available for a limited set of simple building geometries and wind conditions. An alternative method for simulating the local variations around obstacles may be provided by computational fluid dynamic (CFD) models. For example, Dawson et al. (1991) used a three-dimensional numerical code with $k-\varepsilon$ turbulence closure to simulate the transport and diffusion of pollutants over single buildings, and concluded that it is important to account for the local flow variations within the recirculation zone, especially when the pollutant is released within that zone. Letellier et al. (2000) used a CFD model (FLOW3D) to compute wind patterns and plume trajectories within a built-up area, showing that turbulent flow patterns and recirculation cavities created near the buildings will have a significant effect on the downwind transport and dispersion of hazardous materials. Baik and Kim (1999) investigated the flow and pollutant dispersion in urban street canyons by using a two-dimensional numerical code with a $k-\varepsilon$ turbulence closure scheme. For example, they demonstrated that, as the street aspect ratio (ratio of the building height to the width between buildings) increases, instead of having a single vortex in the street canyon, there were two or more stacked vortices of alternating rotation.

A large number of flow and tracer experiments have been performed in fluid modeling facilities and in the field both for single obstacles and for groups of obstacles. For example, Snyder and Lawson (1994) conducted wind tunnel experiments where mean flow patterns were observed for a set of rectangular-shaped blocks immersed in a simulated neutral atmospheric boundary layer. A review by Hosker (1984) was concerned with flow and dispersion around individual or small groups of obstacles. Experiments by Macdonald et al. (1998), Macdonald (2000), Brown et al. (2000), Smith et al. (2000), Baik et al. (2000), and Pavageau and Schatzmann (1999) generally confirm the importance of recirculating vortices within the obstacle arrays or the urban canopy.

In the current paper we use the FEFLO CFD model, described in more detail in Section 3, to examine and attempt to explain the flow patterns observed within the simple obstacle arrays set up in the hydraulic flume described by Macdonald et al. (2000) and summarized in Section 2. The mean flow speed and the turbulence simulated by the numerical model are compared with the experimental observations in Section 4.

2. Description of experiments in hydraulic flume

Observations from the fluid modeling facility at the University of Waterloo (Macdonald et al., 2000) were used to evaluate the CFD numerical model simulations. Four types of arrays of obstacles were studied, including simple square and staggered arrays (see Fig. 1) consisting of cubes with frontal packing densities of $f = 0.16$ and 0.44. The frontal packing density f is a dimensionless ratio defined by

$$f = HW/((S_x + W)(S_y + W)), \quad (1)$$

where the numerator is the frontal area (facing the wind) of an individual obstacle, and the denominator is the "lot area" occupied by a single obstacle. H, W, S_x, S_y denote the height, the width, the streamwise face-to-face spacing and the lateral face-to-face spacing of the obstacles, respectively. Note that $H = W$ for the cubical blocks used as obstacles in this study. Also, the arrays were set up so that $S_y = S_x$. The dimension of the cubes in all the experiments was $H = 50$ mm. S is defined as the cube center-to-center spacing and equals $W + S_y$. The $f = 0.16$ ratio corresponds to a spacing $S_y = 1.5W$, and the $f = 0.44$ ratio corresponds to a spacing of $S_y = 0.5W$.

The flow velocities were measured using an acoustic Doppler velocimeter (Sontek 16 MHz Micro ADV, Serial Number A217). All velocity profiles were measured half-way between two consecutive rows of

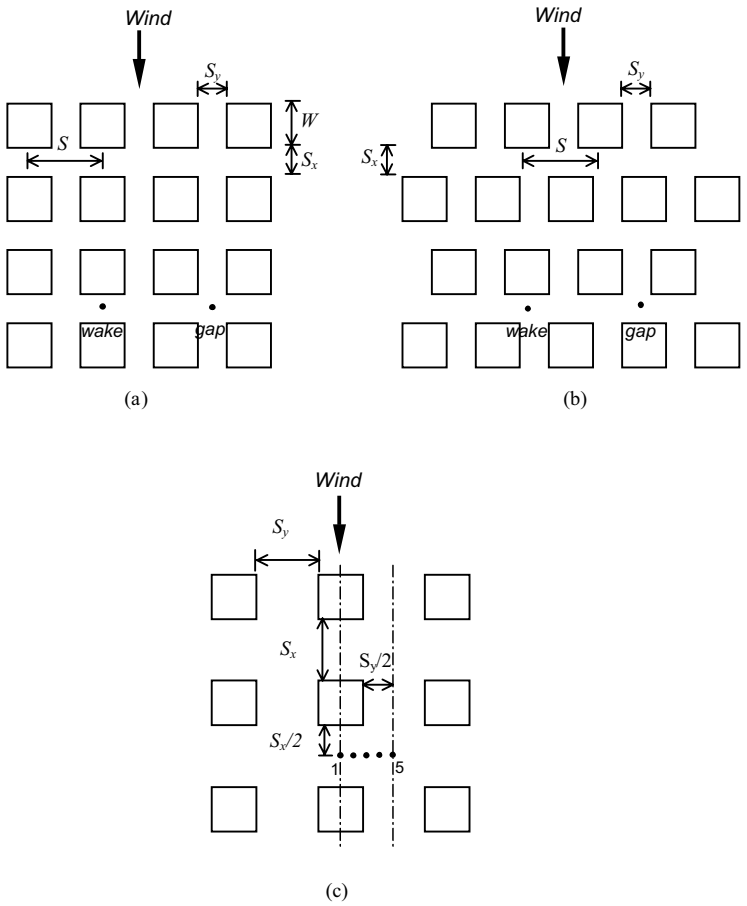

Fig. 1. Schematic diagram of cubical obstacle arrays tested in the hydraulic flume and simulated by the numerical model: (a) square arrays, (b) staggered arrays, (c) locations of vertical profile observations and simulations (location 1 is "in the wake" and location 5 is "in the gap").

obstacles, at five locations shown in Fig. 1c. For some of the comparisons, the profiles were averaged in the lateral direction by using the observations behind an obstacle (i.e., in the wake at location 1 in Fig. 1c) and the observations between the obstacles (i.e., in the lateral gap at location 5 in Fig. 1c). The observations analyzed here included the mean velocity u and the turbulent velocities or standard deviations u_{rms}, v_{rms} and w_{rms}. Each vertical profile consisted of 24 levels ($z/H = 0.1$, 0.2, 0.3, 0.4, 0.5, 0.6, 0.7, 0.8, 0.9, 1.0, 1.1, 1.2, 1.4, 1.6, 1.8, 2.0, 2.4, 2.8, 3.2, 3.6, 4.0, 5.0, 6.0, 8.0, where $H = 50$ mm). The four different test configurations consisted of square arrays with $f = 0.16$, staggered arrays with $f = 0.16$, square arrays with $f = 0.44$ and staggered arrays with $f = 0.44$. The observations typically extended to at least 18 rows, although observations were not made behind all rows.

The profile of mean velocity, u, observed in the incoming (upwind) neutral boundary layer of the hydraulic flume could be approximated by a power-law profile:

$$\frac{u(z)}{u_H} = \left(\frac{z}{H}\right)^{0.29}. \tag{2}$$

The velocity u_H in the incoming flow at the height of the cubes was held constant at 50.5 mm/s. The Reynolds number, based on the height of the obstacles, was $Re_H = 2.5 \times 10^3$ implying that the flow was fully turbulent, as discussed in Snyder and Castro (2002).

3. FEFLO model description

The three-dimensional numerical code used in this study, FEFLO, is based on finite element techniques with unstructured tetrahedral grids (Lohner et al., 2001). These techniques are well suited to the complex geometry of the computational domain and the obstacle

arrays. The time-dependent filtered Navier–Stokes equations of continuity and momentum are solved for an incompressible turbulent flow. A large eddy simulation (LES), using the Smagorinsky closure model, is used to resolve the larger scales of the flow field. Proper turbulence levels are maintained in the model simulations by prescribing time-dependent turbulent velocities on the upstream boundary that agree with the turbulence observed in the hydraulic flume.

The equations solved in LES are developed by filtering the Navier–Stokes equations to remove the small spatial scales. The flow variables are decomposed into large (filtered, resolved) and subgrid (residual, unresolved) scales, respectively. Hence the instantaneous velocity field is given by

$$u_i = \bar{u}_i + u_i',$$

where $i = 1, 2, 3$ represent the x, y, and z components, respectively. The same decomposition is employed for the other flow variables. In LES, the amplitudes of the high-frequency Fourier components of any flow variable F are filtered out or substantially reduced by defining a filtered or resolved field $\bar{F}$ by

$$\bar{F}(x,t) = \int G(x-\xi)F(\xi,t)\,\mathrm{d}^3\xi, \tag{4}$$

where F is the unfiltered variable, G is the filtering function with a characteristic filter scale, Δ_F, which will be used later in the discussion, and the integration is over the entire flow domain, V. For the LES, a spatial average is employed instead of the temporal average used in deriving the Reynolds averaged Navier–Stokes equations.

While the Reynolds averaged Navier–Stokes equations involve a mean field that is stationary, or slowly varying with time, and that varies smoothly in space, the LESs involve fields that are extremely chaotic in space and time. The filtering operator removes only those components of turbulence having spatial scales smaller than the averaging scale (Chen and Jaw, 1998; Hallback et al., 1996). The accuracy of the numerics for the solution to the linear finite elements in the FEFLO model is second order in space and time.

In LES, as with most types of models, the effect of the subgrid-scale stresses must be parameterized. Because the small-scale motion of the turbulence tends to be fairly isotropic and universal (Tennekes and Lumley, 1994), a relatively simple model suffices, if a sufficiently small grid Δ is used. In that case, an eddy viscosity assumption can be made for modeling the subgrid stresses in the LES, namely

$$\Gamma_{ij} = \nu_t\left(\frac{\partial\bar{u}_i}{\partial x_j} + \frac{\partial\bar{u}_j}{\partial x_i}\right) + \frac{1}{3}\Gamma_{ll}\delta_{ij}. \tag{5}$$

The filtered Navier–Stokes equation then reads

$$\frac{\partial\bar{u}_i}{\partial t} + \frac{\partial}{\partial x_j}(\overline{u_i u_j}) = -\frac{1}{\rho}\frac{\partial\bar{p}_i}{\partial x_i} + \frac{\partial}{\partial x_j}\left[(\nu+\nu_t)\left(\frac{\partial\bar{u}_i}{\partial x_j} + \frac{\partial\bar{u}_j}{\partial x_i}\right)\right], \tag{6}$$

$$\bar{P} = \bar{p} - \frac{1}{3}\rho\Gamma_{ll}. \tag{7}$$

The pressure equation is basically a Laplacian and the system is solved with a preconditioned conjugate gradient algorithm. For the isotropic grids, a simple diagonal preconditioner is used.

Following Smagorinsky (1963), and based on Prandtl's mixing length theory, the turbulent viscosity ν_t can be written as

$$\nu_t \sim l^2\frac{\partial U}{\partial y} = (C_s\Delta_f)^2\bar{S}^{1/2}, \tag{8}$$

$$\bar{S} = \frac{1}{2}\left(\frac{\partial\bar{u}_i}{\partial x_j} + \frac{\partial\bar{u}_j}{\partial x_i}\right)\left(\frac{\partial\bar{u}_i}{\partial x_i} + \frac{\partial\bar{u}_j}{\partial x_i}\right), \tag{9}$$

where l is the mixing length of the turbulence and U is the component of the velocity in the primary flow direction. C_s is Smagorinsky's (1963) "constant" which is found to range from 0.1 to 0.24, and is assumed here to have a value of 0.17 (Arya, 1999). The mixing length l is proportional to the filter width Δ_f, which is calculated from the local element size. The average side length of the edges surrounding a point is used for l. There is no special treatment for locations near rooftops or walls, since the element size is usually much smaller along obstacles.

4. Comparisons of numerical simulations with observations

The numerical model predictions were compared to the set of hydraulic flume observations. The numerical simulations were performed at experiment scale. A minimum averaging time of 2 min was employed to insure stable results for the mean velocities and turbulent intensities. The averaging times were similar for the model predictions and the hydraulic flume observations.

Two types of vertical profiles are used in the comparisons in this section. One type of profile is a single profile taken at a specific measurement location, usually behind one obstacle or in the gap between two obstacles (locations 1 or 5 in Fig. 1c). The other type of profile is a laterally averaged profile that is calculated as the average of the two single profiles described in the previous sentence, and is useful for example to estimate the average transport and dispersion. Taking advantage of the symmetry of the array, the vertical profiles were spatially averaged in the y-direction, using the equation

$$u(z) = (Wu_c(z) + S_y u_g(z))/(W + S_y), \tag{10}$$

where W is the width of the cube and S_y is the face-to-face spacing between two adjacent cubes. u_g is the wind

speed in the gap and u_c is the wind speed in the cavity or wake behind the cube. This procedure is analogous to that used by Macdonald et al. (2000) for deriving the laterally averaged experimental wind speed profiles. For a configuration consisting of nonuniform arrays it would be necessary to use many more velocity profiles to insure stable averages.

It would be desirable to compare the numerical simulations at a given row with the observations at the same row, where the row number refers to the number of rows of obstacles encountered by the flow in the downwind direction. However, the numerical simulations were stopped after eight rows (due to time constraints for the model runs), while the experiments extended for 18 or more rows. Because observations were not taken after each row, it was usually not possible to compare the numerical simulations and observations at the same row, as seen in many of the figures in this section. In most cases, this is not a problem, since Macdonald et al. (2000) report that, in the water flume, the mean flow and the turbulence fields approached equilibrium values after typically three rows of obstacles. The same near-equilibrium is also found in the numerical results after about three or four rows.

4.1. Specification of the incoming boundary layer

The mean velocity profile for the incoming (upwind) neutral boundary layer was prescribed for the numerical simulations using a power-law profile with an exponent of 0.29. This value is similar to the fitted values in the experiments and is typical of wind speed profiles over urban terrain (Davenport, 1963). For all the analyses below, the mean velocities and the turbulent standard deviations are scaled by $u_H = 50.5$ mm/s, which is the mean velocity of the incoming boundary layer at height H, and was used in all experiments and numerical simulations. This scaling method is a standard procedure in analysis of observations in fluid models. To approximate the time-dependent turbulence of the incoming (upwind) flow for input to the numerical simulations, a time series of turbulent velocities was generated using a Monte Carlo model. The turbulent component, u', of the total velocity is assumed to be the sum of the correlated component and a random or Monte Carlo component u''. The random component is assumed to have a Gaussian distribution with zero mean and variance, $u^2_{f\mathrm{rms}}$, given by

$$u'(t) = u'(t - \Delta t)R(t) + u'', \tag{11}$$

$$u^2_{f\mathrm{rms}} = u^2_{\mathrm{rms}}[1 - R^2(\Delta t)]. \tag{12}$$

The autocorrelation function $R(\Delta t)$ is assumed to be given by the exponential formula

$$R(t) = \exp\left(\frac{-t}{T}\right). \tag{13}$$

The Lagrangian time scale, T, of the flow is assumed to be proportional to H.

The values of u_{rms}, v_{rms}, and w_{rms} observed in the hydraulic flume in the approach flow at the entrance of the test section were used in the above equations to generate a realistic fluctuating time series for the turbulent components. This time series of turbulent velocity components was added to the mean flow at the inflow boundary of the computational domain. If the assumed incoming flow did not have this turbulent variability, the CFD model would not produce and maintain sufficient turbulent energy within the domain of the solution.

The conditions assumed in the numerical model for the other boundaries are as follows: For bodies immersed in the flow (walls, floors, obstacles), the normal velocity equals 0.0 at the surface and the wind shear at the surface is estimated from the standard logarithmic wind speed profile. For the downwind outflow boundary, the pressure is prescribed and the velocity is extrapolated. For the top boundary, the pressure is prescribed and the normal velocity may be nonzero.

4.2. Comparison of simulated and observed mean and turbulent velocity profiles in the $f = 0.16$ square arrays

Velocity profiles for the test case with a frontal packing density of $f = 0.16$ (i.e., a face-to-face spacing, S_y, of $1.5H = 1.5W$ between obstacles) and a square array configuration (see Fig. 1a) were simulated by the FEFLO model for an array with eight rows. Fig. 2 compares numerical simulations and observations for the laterally averaged normalized mean velocity profiles for several rows. Both the observed and simulated laterally averaged normalized mean velocity profiles appear to reach an equilibrium state beyond row 4, with only slight variations with downwind distance.

As can be seen from Fig. 2, there is a difference in the normalized mean velocity, u/u_H, of about 10% or 20% or less among the various velocity profiles at a given z/H. At a higher z/H of about 3 or 4, there is seen to be a mean overprediction bias of about 10%, possibly due to differences in the interactions of the flow with the upper boundary in the computational domain and in the hydraulic flume. At heights less than $z/H = 1$, where the mean flow speeds are low, the discrepancies between the numerical simulations and the observations are typically 30%. Both observations and simulations show the greatest velocity shear near and just above the tops of the obstacles (i.e., at $z/H \approx 1.0$), with much less shear at heights within the obstacles (i.e., at $z/H \approx 0.5$).

Fig. 3 compares the mean simulated and observed normalized velocity profiles at single locations, directly behind a cube (i.e., in a wake or a recirculating cavity) and behind a gap. Lower mean normalized velocities (by about 50%) are simulated and observed in the wakes behind the cubes than in the gaps, as expected from

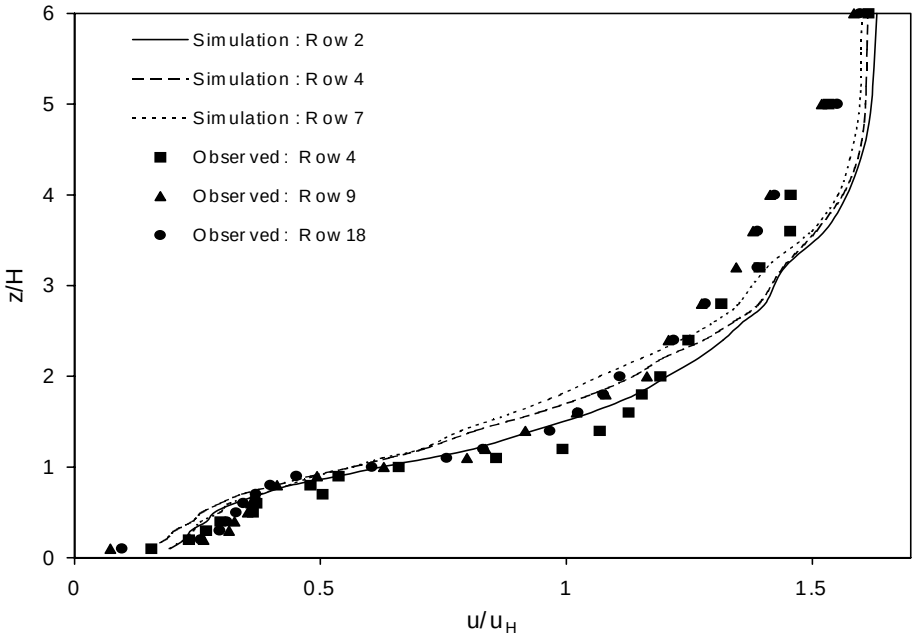

Fig. 2. Comparison of laterally averaged mean velocity profiles for a square array configuration with frontal packing density, f, of 0.16: numerical simulation (lines) and observed (symbols).

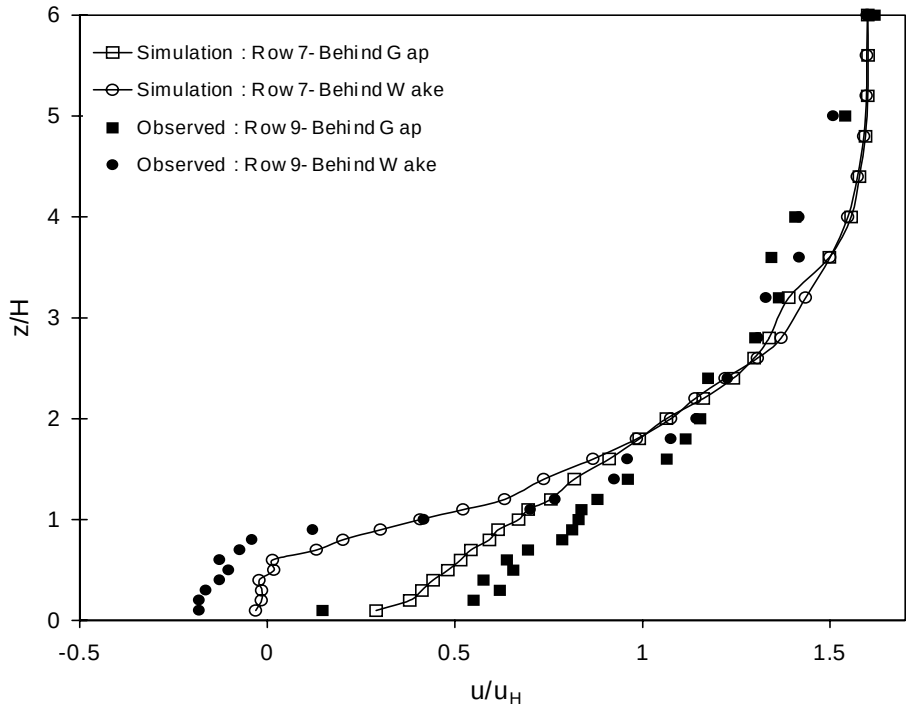

Fig. 3. Comparison of the mean velocity profiles behind a cube in the wake (circles) and in a gap (squares) for the $f = 0.16$ square array configuration: numerical simulation (open symbols) and observed (closed symbols).

intuition. Negative mean velocities (i.e., upstream flow directions) are observed at $z/H<0.8$ in the wake or recirculation zone behind the cube. This upstream flow is also simulated by the model, although the magnitudes of the simulated flow speeds are less. At $z/H>1.5$, there is little difference between the u/u_H values behind the cubes and in the gaps.

The nondimensional turbulent intensities, u_{rms}/u_H, v_{rms}/u_H, and w_{rms}/u_H are plotted versus z/H in Fig. 4, for lateral averages. The simulated turbulence intensities are generally less than the observed values by about 40% but still obey the hierarchy $u_{rms}>v_{rms}>w_{rms}$, in agreement with general relations in texts such as Stull (1997). The simulated and observed turbulence intensities generally are largest at one or two z/H, and are reduced to about $\frac{1}{2}$ of their maximum values at $z/H<1.0$, in agreement with other field and laboratory observations reported by Rotach (1997) and Hanna and Britter (2002).

4.3. Comparison of simulated and observed mean and turbulent velocity profiles in the $f=0.16$ staggered arrays

The previous subsection dealt with the $f=0.16$ square array (see Fig. 1a), whereas this subsection presents similar results for the staggered array (see Fig. 1b). In both cases the face-to-face obstacle spacing, S_y, is $1.5W=1.5H$. For the numerical simulations and the observations, the mean relative velocity, u/u_H, is found to be less at $z/H<1.0$ in the staggered array because of the reduced presence of channeled flow in "street canyons" between the obstacles. This effect is less pronounced in the experiments. The laterally averaged vertical profiles of mean relative velocity, u/u_H, suggest larger differences in the simulated versus observed values for the staggered array at $z/H<1$, with an underprediction by about 30–90%.

The simulated and observed individual normalized mean velocity profiles behind a cube centerline (wake) and behind a gap in the $f=0.16$ staggered array configuration for the 7th row (simulated) and the 9th row (observed) were also compared. For $z/H<1.0$ and within the wake region, there is good agreement between the numerical simulations and the observations. As in Fig. 3, negative (upstream-directed) mean velocities are seen in the wake region. For the data in the gap at $z/H<2$, there is an underprediction by about 30–50%.

Fig. 5 compares the simulated mean relative velocity, u/u_H, profiles for the square and staggered array configuration behind a cube centerline (wake) and in the gap for the 7th row of an $f=0.16$ array. As mentioned earlier, since the cubes are not aligned right behind each other in the staggered array configuration, there is a sheltering effect that causes the "gap" velocities at $z/H<1$ to be less (by about 50% or more) for the staggered array than for the square array. The flow in the gaps in the square arrays tends to be relatively unimpeded in the longitudinally oriented "street canyons" between the cubes.

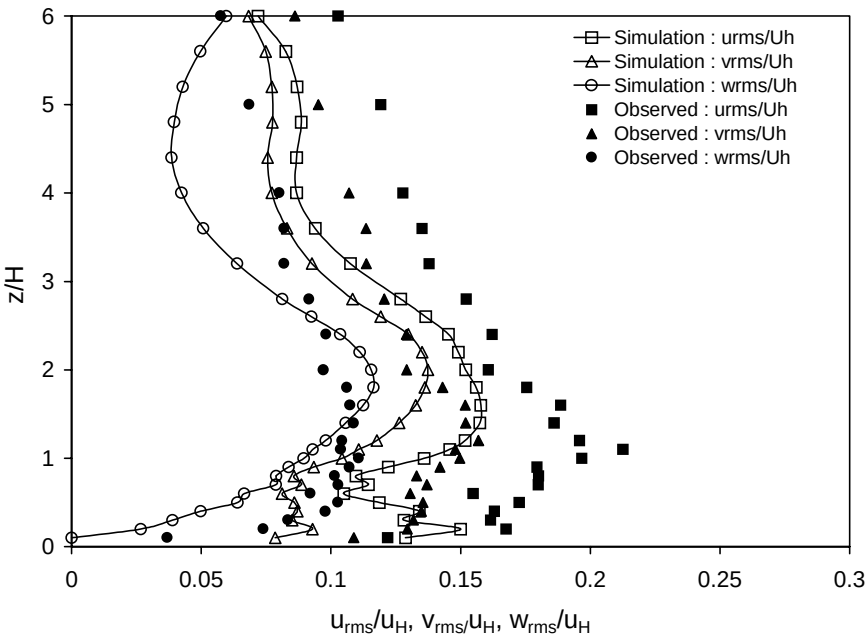

Fig. 4. Comparison of laterally averaged vertical profiles for turbulent intensities of the $f=0.16$ square array configuration: numerical simulation (open symbols with line) behind the 7th row and observed (closed symbols) behind the 18th row.

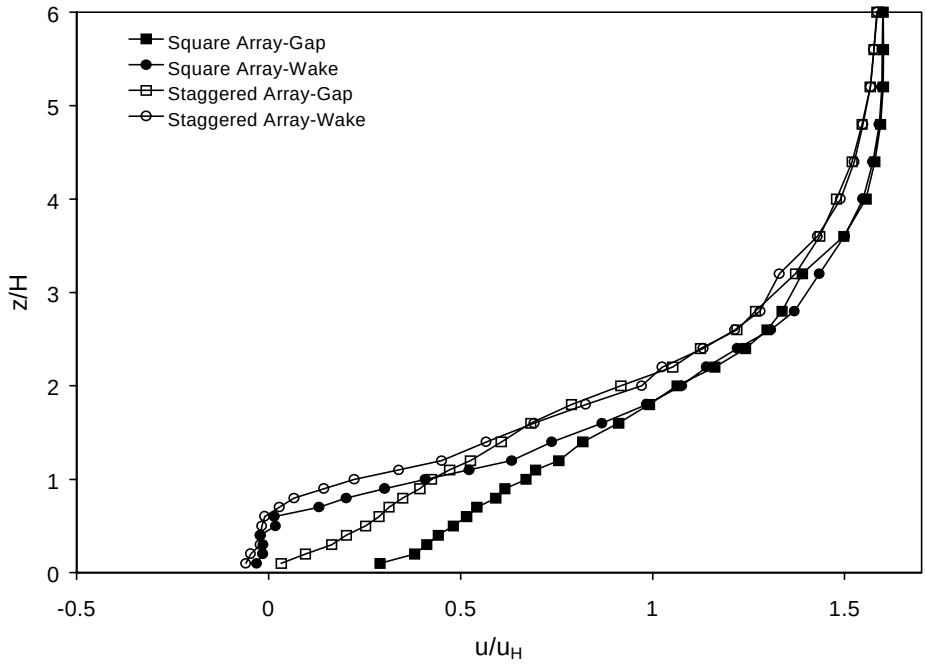

Fig. 5. Comparison of the numerically simulated mean velocity profiles behind a cube centerline or wake (circles) and behind a gap (squares) in the 7th row of an $f = 0.16$ array in a square (solid symbols) and staggered (open symbols) configuration.

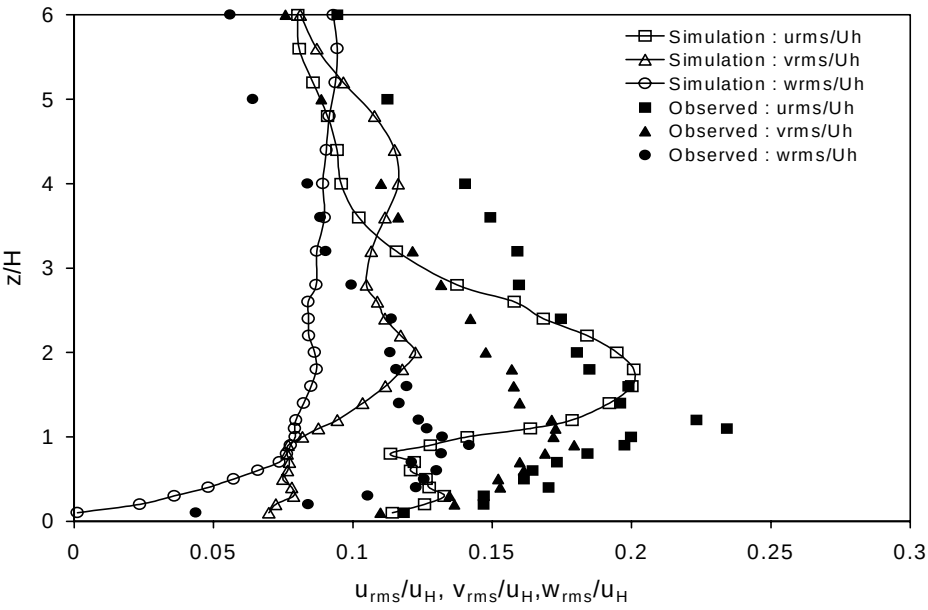

Fig. 6. Laterally averaged profiles for turbulent intensities of the $f = 0.16$ staggered array configuration: numerical simulation (open symbols with line) behind the 7th row and observed (closed symbols) behind the 18th row. The u, v, and w components are denoted by squares, triangles, and circles, respectively.

Fig. 6 shows model-simulated and observed laterally averaged turbulent intensities for the staggered array configuration. In general, there is an underprediction of about a factor of 2 at $z/H = 1$. The largest discrepancy between the simulations and the observations is found for the vertical turbulent intensity, w_{rms}/u_H, at heights approaching zero, where the simulated vertical turbulence intensity approaches zero, while the observed

vertical turbulence intensity does not fall below 0.5. These turbulence results for the staggered array can be compared with those for a square array in Fig. 4, which also shows underpredictions. However, as stated earlier, it is very difficult to maintain the proper turbulence intensities in a numerical model, and more improvements are needed.

4.4. Comparison of simulated and observed mean and turbulent velocity profiles in the $f = 0.44$ square arrays

A similar analysis has been performed for simulated and observed configurations with a frontal packing density of $f = 0.44$. This array has the obstacles relatively close together, with face-to-face spacings, S_y, of only $0.5W = 0.5H$. Experimental data were only available for $z/H > 0.6$ since there was insufficient room for the acoustic probe to descend into the narrow gaps. As the packing density is increased from 0.16 to 0.44 (i.e., as the spacing between cubes is decreased from $1.5W$ to $0.5W$), the laterally averaged relative mean wind speed, u/u_H, in the canopy ($z/H < 1$) is found to decrease by about a factor of three in both the numerical simulations and the observations. The numerical simulations generally indicate a smaller wind shear at the height of the obstacles (i.e., at $z/H = 1$) than the observations. For both $f = 0.16$ and 0.44, the simulated and observed mean velocities at $z/H < 0.8$ are in good agreement (within about 10% or 20%).

Fig. 7 compares the simulated and observed laterally averaged longitudinal turbulent intensity, u_{rms}/u_H, for the $f = 0.16$ and 0.44 square array configurations. It is seen that, at $z/H < 1$ (within the canopy), as the packing density increases from $f = 0.16$ to 0.44, the longitudinal turbulent intensity decreases by about 30% or 40%, for both the numerical simulations and the observations. However, it should be noted that the normalizing velocity, u_H, does not change from the $f = 0.16$ to the $f = 0.44$ arrays and is 50 mm/s in both arrays. This decrease of turbulence intensity as f increases may not occur if the local wind speed were used as the normalizing velocity for the turbulence intensity rather than the inflow value of u_H. Furthermore, the square and circle symbols in Fig. 7 show that the model simulations of u_{rms}/u_H are about 20–40% less than the observations for both arrays.

4.5. Comparison of simulated and observed mean and turbulent velocity profiles in the $f = 0.44$ staggered arrays

Fig. 8 compares the simulated mean relative velocity profiles in a wake and in a gap in the 7th row of the $f = 0.44$ array (with face-to-face spacing, S_y, of $0.5W$) for the square and staggered array configurations. The lateral variability of the mean velocity profiles is slightly reduced for the staggered array configuration. This behavior was also shown in Fig. 9 for the $f = 0.16$ array configuration and is probably due

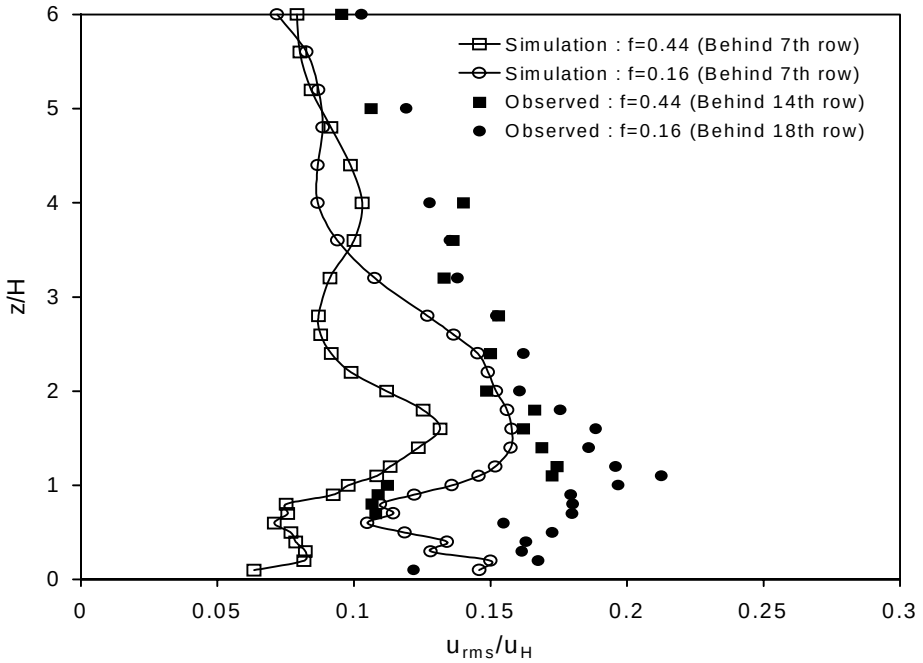

Fig. 7. Comparison of laterally averaged vertical profiles for longitudinal turbulent intensity: numerical simulation (open symbols with line) and observed (closed symbols) for the $f = 0.16$ (circles) and $f = 0.44$ (squares) square array configurations.

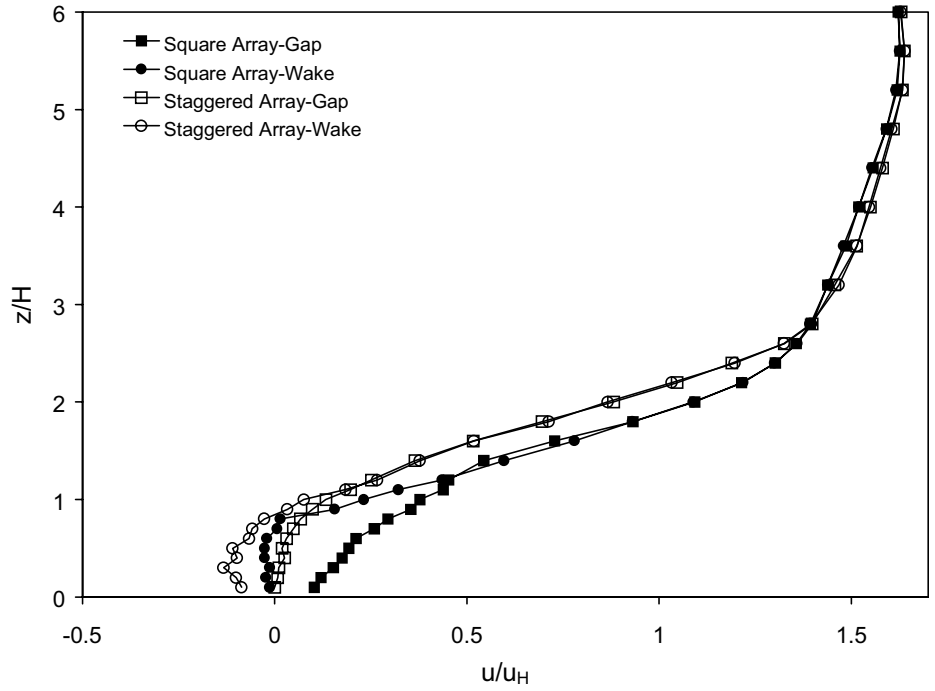

Fig. 8. Comparison of the simulated mean velocity profiles behind a cube centerline or wake (circles) and behind a gap (squares) in the 7th row of an $f = 0.44$ array in a square (solid symbols) and staggered (open symbols) configuration.

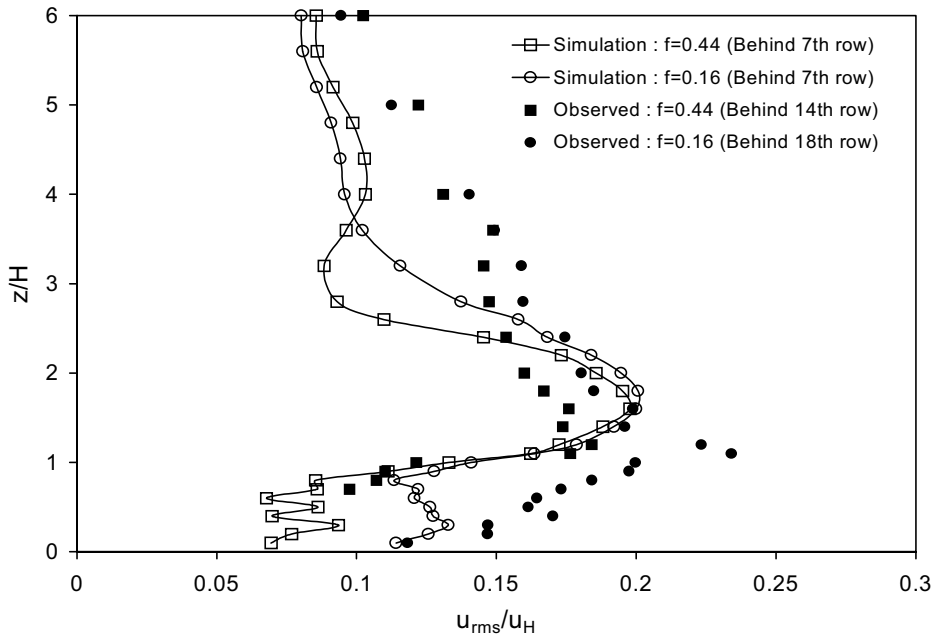

Fig. 9. Comparison of laterally averaged vertical profiles of longitudinal turbulent intensity for numerical simulation (open symbols) and observed (closed symbols) for the $f = 0.16$ (circles) and $f = 0.44$ (squares) staggered array configurations.

to the fact that longitudinally oriented "street canyons" appear in the square arrays but not as much in the staggered arrays. Note that at $z/H > 1$, there is little difference in the simulated mean relative velocities in the gap and wake positions for either the square or staggered array.

The simulated and observed laterally averaged mean relative velocity profiles were compared for the $f = 0.16$ and 0.44 staggered array configurations. As for the square array configurations, when the packing density is increased from $f = 0.16$ to 0.44, the mean relative wind speed in the canopy is decreased by over 50%. The mean relative velocities tend to be underpredicted by about 20–40% at $z/H < 2$.

The simulated laterally averaged longitudinal turbulent intensity, u_{rms}/u_H, is compared with observations in Fig. 9 for the $f = 0.16$ and 0.44 staggered array configurations. The longitudinal turbulent intensities for the $f = 0.16$ and 0.44 staggered arrays are similar in magnitude to their counterparts for the square arrays shown in Fig. 7, with the exception that, at $z/H \approx 1.5$, the turbulent intensities for the staggered arrays are about 30% or 40% larger than those for the square arrays. This difference could be attributed to the effects of the increased obstructions of the obstacles in the staggered array configuration. In Fig. 9, the numerical simulation underpredicts by about 10–40% at $z/H > 3$ and overpredicts by about 10% at $z/H \approx 1.5$ for both array configurations. At $z/H < 1$, the simulation tends to underpredict by about 10–50% for $f = 0.16$ and there are not enough data to form conclusions for $f = 0.44$ (since the acoustic probe cannot be brought lower than $0.6H$).

As mentioned earlier, there are differences seen in the figures in this section in the row numbers from which the numerical simulations and the observations are taken. This is due to the fact that the simulations did not proceed past row 8 and the observations were taken only at certain rows. However, the effects of these differences are expected to be minimal, since both the observations and the simulations appeared to reach an equilibrium past row 3 or 4.

5. Summary

The flow fields around four series of cubical array configurations were studied using a three-dimensional numerical code, FEFLO, based on finite element techniques with unstructured tetrahedral grids. The model was run in large eddy simulation (LES) mode using the Smagorinsky subgrid closure model. As inputs to the numerical simulation, a power-law profile was assumed for the mean wind flow and turbulent fluctuations were approximated using a Monte Carlo approach at the upwind boundary. The four test cases involved square and staggered cubical array configurations with height H (equal to width W) and two different face-to-face spacings, S_y, ($0.5W$ and $1.5W$) between obstacles. The numerical simulations were limited to 8 rows of obstacles due to computational constraints. The numerical simulations were evaluated with a set of observations (Macdonald et al., 2000) from a hydraulic water flume at the University of Waterloo, where the four sets of geometrical arrangements of the cubes were the same as those for the simulations. In both the simulations and the observations, after about three rows, the canopy velocity profiles adapted very quickly to a near-equilibrium state.

It was seen that model-simulated laterally averaged relative mean velocity, u/u_H, profiles generally agree with the hydraulic flume observations within about $+40\%$. The numerical simulations were able to satisfactorily simulate the main characteristics of the observations, such as the large shear in the mean wind speeds and the maximum in the turbulence at the top of the obstacles (i.e., at $z/H \approx 1.0$), and the relatively constant mean wind speed and the lower turbulence (standard deviations equal to about $\frac{1}{2}$ of those at $z/H = 1.0$) within the obstacle canopy at $z/H \approx 0.5$.

In the square array configuration, the wind flow at $z/H < 1.0$ was in the upstream direction in the wakes behind the obstacles, and tended to be channeled into the gaps in the so-called "street canyon" between the obstacles. In the staggered array configuration, the channeling effect in the street canyon was reduced. The numerical simulations were able to simulate this behavior although there were sometimes underpredictions of about 30% at $z/H < 1.0$. Also, the lateral variability of the mean normalized velocity (that is, the difference between the "wake" and the "gap" flow) was reduced for the staggered configuration compared to the square array configuration. The lateral variability was strongest at the lowest heights and disappeared at $z/H > 1.5$. As the obstacle spacing decreased from $1.5W$ to $0.5W$ (i.e., frontal packing density increased from 0.16 to 0.44), the mean normalized wind speeds decreased by a factor of three at $z/H < 1.0$, although the turbulent velocities were little changed.

The simulated turbulent intensities showed a general tendency towards underprediction by about 30% or 40%. However, the relative variations of turbulence intensities with height and with array configuration were correctly simulated by the numerical model. The difficulties of simulating the relatively high turbulent intensities in an atmospheric boundary layer with a CFD model are well known, and it is felt that this model application exercise represents a substantial improvement over many prior applications.

This first series of numerical large eddy simulations (LESs) of the flow and turbulence field has shown the feasibility of this type of simulation in the complex

geometry formed by a regular array of obstacles and has allowed us to identify the areas of improvement. Our next step will be to carry out similar comparisons but for the numerical simulation of the dispersion of material in the obstacle array, which is the ultimate goal of this work. This has already started with results from the experimental facility (Macdonald et al., 2001).

Acknowledgements

This research was supported by the US Defense Threat Reduction Agency (DTRA). The technical contract monitors were Major Thomas Smith, Mr. Ronald Meris, and Major Brian Beitler. The authors thank Rex Britter of Cambridge University and Fernando Camelli of George Mason University for useful discussions of these simulations.

References

Arya, S.P., 1999. Air Pollution Meteorology and Dispersion. Oxford University Press, New York, 310pp.

Baik, J., Kim, J., 1999. A numerical study of flow and pollutant dispersion characteristics in urban street canyons. Journal of Applied Meteorology 38, 1576–1589.

Baik, J., Park, R., Chun, H., Kim, J., 2000. An experimental investigation of urban street canyon flows. 11th Joint Conference on the Applications of Air Pollution Meteorology with the A&WMA, AMS, 45 Beacon Street, Boston 02108, pp. 59–64.

Brown, M.J., Lawson Jr., R.E., DeCroix, D.S., Lee, R.L., 2000. Mean flow and turbulence measurements around a 2-D array of buildings in a wind-tunnel. 11th Joint Conference on the Applications of Air Pollution Meteorology with the A&WMA, AMS, 45 Beacon Street, Boston 02108, pp. 35–41.

Calhoun, R., Chan, S., Leone, R.L., Shinn, J., Stevens, D., 2000. Flow patterns around a complex building. 11th Joint Conference on the Applications of Air Pollution Meteorology with the A&WMA, AMS, 45 Beacon Street, Boston 02108, pp. 47–52.

Chen, C.L., Jaw, S.Y., 1998. Fundamentals of Turbulence Modeling. Taylor & Francis, Washington, DC, pp. 225–267.

Dawson, P., Stock, D.E., Lamb, B., 1991. The numerical simulation of airflow and dispersion in three-dimensional atmospheric recirculation zones. Journal of Applied Meteorology 30, 1005–1024.

Davenport, A.G., 1963. The relationship of wind structures to wind loading. Proceedings of the Conference on Buildings and Structures, NPL Laboratory, England, pp. 54–83.

DeCroix, D.S., Smith, W.S., Streit, G.E., Brown, M.J., 2000. Large eddy and Gaussian simulations of downwind dispersion from large building HVAC exhaust. 11th Joint Conference on the Applications of Air Pollution Meteorology with the A&WMA, AMS, 45 Beacon Street, Boston 02108, pp. 53–58.

Hallback, M., Henningson, D.S., Johansson, A.V., Alfredsson, P.H., 1996. Turbulence and Transition Modeling. Kluwer Academic Publishers, Dordrecht, pp. 201–224.

Hanna, S.R., Britter, R.E., 2002. Flow and Vapor Cloud Dispersion at Industrial and Urban Sites. ISBN 0-8169-0863-X, AIChE, 3 Park Avenue, New York, NY 10016-5901, 140pp.

Hosker, R.P., 1984. Flow and diffusion near obstacles. In: Randerson, D. (Ed.), Atmospheric Science and Power Production, Publication DOE/TIC-27601. Technical Information Center, US DOE, pp. 241–326.

Kastner-Klein, P., Plate, E.J., 1999. Wind-tunnel study of concentration fields in street canyons. Atmospheric Environment 33, 3973–3979.

Letellier, B., Restrepo, L., Shaffer, C.J., 2000. Near-field dispersion of fission products in complex terrain using a 3-D turbulent fluid-flow model. 11th Joint Conference on the Applications of Air Pollution Meteorology with the A&WMA, AMS, 45 Beacon Street, Boston 02108, pp. 381–397.

Lohner, R., Yang, C., Cebral, J., Soto, O., Camelli, F., Baum, J.D., Luo, H., Mestreau, E., Shavov, D., Ramamurti, R., Sandberg, W., Oh, C., 2001. Advances is FEFLO. AIAA-01-0592.

Macdonald, R.W., 2000. Modeling the mean velocity profile in the urban canopy layer. Boundary Layer Meteorology 97, 25–45.

Macdonald, R.W., Griffiths, R.F., Hall, D.J., 1998. A comparison of results from scaled field and wind tunnel modeling of dispersion in arrays of obstacles. Atmospheric Environment 32, 3845–3862.

Macdonald, R.W., Carter, S., Slawson, P.R., 2000. Measurements of mean velocity and turbulence statistics in simple obstacle arrays at 1:200 scale. Department of Mechanical Engineering, University of Waterloo, hermal Fluids Report 2000-1.

Macdonald, R.W., Carter-Schofield, S., Slawson, P.R., 2001. Measurements of mean plume dispersion in simple obstacle arrays. Department of Mechanical Engineering, University of Waterloo, Thermal Fluids Report 2001-2.

Oke, T., 1987. Boundary Layer Climates, 2nd Edition. Halsted, New York.

Pavageau, M., Schatzmann, M., 1999. Wind tunnel measurements of concentration fluctuations in an urban street canyon. Atmospheric Environment 33, 3961–3971.

Rotach, M.W., 1997. The turbulence structure in an urban roughness sublayer. In: Perkins, R.J., Belcher, S.E. (Eds.), Flow and Dispersion through Groups of Obstacles. Clarendon Press, Oxford, pp. 143–155.

Smagorinsky, J., 1963. General circulation experiments with the primitive equations. Part I: The basic experiment. Monthly Weather Review 91, 99–152.

Smith, W.S., Reisner, J.M., Decroix, D.S., Brown, M.J., Lee, R.L., Chan, S.T., Stevens, D.E., 2000. A CFD model intercomparison and validation using high resolution wind tunnel data. 11th Joint Conference on the Applications of Air Pollution Meteorology with the A&WMA, AMS, 45 Beacon Street, Boston 02108, pp. 41–46.

Snyder, W.H., Castro, I.P., 2002. The critical Reynolds number for rough wall boundary layers. Journal of Wind Engineering and Industrial Aerodynamics 90, 41–54.

Snyder, W.H, Lawson Jr., R.E., 1994. Wind-tunnel measurements of flow fields in the vicinity of buildings. Eighth Joint Conference on the Applications of Air Pollution Meteorology with the A&WMA, AMS, 45 Beacon Street, Boston 02108, pp. 244–250.

Stull, R.B., 1997. An Introduction to Boundary Layer Meteorology. Kluwer Academic Publishers, Boston, 670pp.

Tennekes, H., Lumley, J.L., 1994. A First Course in Turbulence. The MIT Press, Cambridge, MA, pp. 256–290.